

This is the accepted manuscript made available via CHORUS. The article has been published as:

Two-Dimensional π -Conjugated Covalent-Organic Frameworks as Quantum Anomalous Hall Topological Insulators

Liang Dong, Youngkuk Kim, Dequan Er, Andrew M. Rappe, and Vivek B. Shenoy

Phys. Rev. Lett. **116**, 096601 — Published 29 February 2016

DOI: [10.1103/PhysRevLett.116.096601](https://doi.org/10.1103/PhysRevLett.116.096601)

2-Dimensional π -conjugated covalent-organic frameworks as quantum anomalous Hall topological insulators

Liang Dong¹, Youngkuk Kim², Dequan Er¹, Andrew M. Rappe², and Vivek B. Shenoy^{1,*}

¹*Department of Materials Science and Engineering, University of Pennsylvania, Philadelphia, PA 19104, USA*

²*The Makineni Theoretical Laboratories, Department of Chemistry, University of Pennsylvania, Philadelphia, Pennsylvania 19104-6323, USA*

** Corresponding Author, Email: vshenoy@seas.upenn.edu*

Abstract

The quantum anomalous Hall (QAH) insulator is a novel topological state of matter characterized by a non-zero quantized Hall conductivity without an external magnetic field. Using first-principles calculations, we predict the QAH state in monolayers of covalent-organic frameworks based on the newly synthesized $X_3(C_{18}H_{12}N_6)_2$ structure where X represents 5d transition metal elements Ta, Re, and Ir. The π -conjugation between X d_{xz} and d_{yz} orbitals, mediated by N p_z and C p_z orbitals, gives rise to a massive Dirac spectrum in momentum space with a band gap of up to 24 meV due to strong spin-orbit coupling. We show that the QAH state can appear by chemically engineering the exchange field and the Fermi level in the monolayer structure, resulting in non-zero Chern numbers. Our results suggest a reliable pathway toward the realization of a QAH phase at temperatures between 100K and room temperature in covalent-organic frameworks.

Two-dimensional (2D) topological insulators (TIs) are currently creating a surge of research activity [1-5]. In the presence of time-reversal symmetry (TRS), spin-orbit coupling (SOC) locks the momentum and spin directions of electrons in the metallic edge states of 2D TIs, leading to the quantum spin Hall (QSH) effect [6,7]. On the other hand, when a ferromagnetic (FM) exchange interaction is introduced, TRS is broken and the chemical potentials of two metallic channels with opposite spin polarizations can be unbalanced, giving rise to the quantum anomalous Hall (QAH) effect. The spin-polarized edge electron channel of QAH insulators is of crucial importance because of its incredibly precise quantization, robustness against defects, disorder and surface contamination over hundreds of micrometers, and relatively low energy consumption [6], which are highly promising in spintronic devices, quantum computation, and low-power electronic devices.

The study of the QAH effect is still in its formative stage, due to the lack of suitable material realizations. Although the QAH phase has been observed in Cr- or V-doped $(\text{Bi,Sb})_2\text{Te}_3$ thin films, it survives only at low temperatures ($\approx 30\text{-}85\text{ mK}$) [8-11], and the Hall conductance completely vanishes when the temperature is above 2K [8,10,11]. Moreover, the molecular beam epitaxy synthesis method of such thin films [8-11] is expensive and thus inadequate for mass production. To date, diverse inorganic [12-19] and organic [20] materials have been theoretically proposed for the QAH effect, but the experimental observation based on these materials remains elusive due to their generic structural complexity [21,22]. Therefore, it is imperative to find more stable materials that can be fabricated using easy and inexpensive methods. Here we propose that organic 2D π -conjugated polymer networks could satisfy these criteria as they can be synthesized using chemical solution or vapor deposition techniques [23]. Most importantly, it is feasible to manipulate their molecular structure and the chemical elements of functional

groups for desired orbital hybridization, magnetic exchange field, and/or SOC strength, all of which are essential ingredients to realize the QAH effect.

In this Letter, we demonstrate that the QAH phase can be achieved by rationally engineering the structure of the newly synthesized $X_3(\text{HITP})_2$ covalent-organic framework (COF), where X is a transition metal and HITP is the 2,3,6,7,10,11-hexaiminotriphenylene ($\text{C}_{18}\text{H}_{12}\text{N}_6$) functional group [24,25]. We carry out density functional theory (DFT) calculations to show that a proper $5d$ transition metal element (Ta, Re, or Ir) in an $X_3(\text{HITP})_2$ monolayer gives rise to both a FM exchange field and strong SOC. To drive the system into a QAH insulating phase, the N atoms in the HITP functional group are fully or partially replaced by O atoms to tune the Fermi level (E_f), so that the occupied bands have a non-zero Chern number. Our calculations show that the QAH effect can be realized if $X=\text{Ta}$ and all N atoms are replaced by O atoms [*i.e.*, in $\text{Ta}_3(\text{C}_{18}\text{H}_{12}\text{O}_6)_2$]. With E_f resides in an SOC-induced band gap of 24 meV, $\text{Ta}_3(\text{C}_{18}\text{H}_{12}\text{O}_6)_2$ can potentially host the QAH state at much higher temperatures than that of the previously reported QAH experiments [8-10]. Another system that can host QAH effect is $\text{Ir}_3(\text{C}_{18}\text{H}_{12}\text{N}_3\text{O}_3)_2$ (*i.e.*, $X=\text{Ir}$ and half of the N atoms are replaced by O atoms), wherein E_f can be tuned to within an SOC-induced band gap (8 meV) via electric gating, enabling a gate-voltage tunable QAH effect. These results indicate that the structural derivatives of $X_3(\text{HITP})_2$ are promising material realizations of a 2D magnetic TI. We expect that these materials can expedite experimental research in the QAH effect and its practical applications in electronic devices.

Our DFT calculations are performed using the VASP code [26] with projector augmented wave pseudopotentials [27] and Perdew–Burke–Ernzerhof generalized gradient approximation (PBE-GGA) [28]. Other computational details can be seen in Supplemental Material [29]. All atoms in $X_3(\text{HITP})_2$ monolayers are coplanar [Fig. 1(a)], thus preserving the mirror symmetry

(M_z) about the basal plane. The three X atoms per unit cell form a kagome lattice [Fig. 1(b)]. Among this material family, $\text{Ni}_3(\text{HITP})_2$ and $\text{Cu}_3(\text{HITP})_2$ have been recently synthesized via solution-based chemical reactions and isolated via extensive washing [24,25]. Therefore, we believe that $\text{X}_3(\text{HITP})_2$ with other transition metal elements should be accessible using similar processes. In this study, we focus on $\text{X}_3(\text{HITP})_2$ where X is a 5d transition metal from Hf to Au, as they are heavier, and hence have stronger SOC. The lattice parameters $|\mathbf{a}_1|=|\mathbf{a}_2|\equiv a$ of $\text{Ni}_3(\text{HITP})_2$ and $\text{Cu}_3(\text{HITP})_2$ are calculated as 21.91 Å and 21.75 Å, respectively, agreeing well with previous DFT studies [24,25,38,39]. a for X=5d transition metal elements is listed in Table S1 in Supplemental Material [29].

We first consider the magnetic configurations of $\text{X}_3(\text{HITP})_2$. Our calculations show that it energetically favors an FM state with a spontaneous magnetic moment $\mu=1 \mu_B$ per X atom, where X has an odd number of valence electrons n_X (X=Ta, Re, Ir, or Au, see Table S1 in Supplemental Material [29]); while it favors a non-magnetic ground state for X with an even n_X (X=Hf, W, Os, or Pt). The origin of magnetism can be understood from the low-energy band configurations (Fig. 2). States near E_f comprise of the X 5d atomic orbitals and the HITP s and p orbitals. Each X atom is surrounded by four nearest-neighbor nitrogen atoms, generating a deformed square planar crystal field in the basal (N-N distance in the y -direction is longer than that in the x -direction, Fig. 2). By the crystal field, the X 5d orbitals ($d^{A,B,C}$) split into five distinct energy levels, denoted by $d_{xz}^{A,B,C}$, $d_{yz}^{A,B,C}$, $d_{z^2}^{A,B,C}$, $d_{x^2-y^2}^{A,B,C}$, and $d_{xy}^{A,B,C}$ from the lowest to the highest in the energy spectrum. The N p_z orbitals form π -bonds with the X $d_{xz}^{A,B,C}$ and $d_{yz}^{A,B,C}$ orbitals, due to the same odd parity under M_z about the xy -plane, while the other d orbitals, which have an even parity of M_z , do not join the π -bond network of HITP. The interaction between p_z and d_{xz} and d_{yz} produces lower-lying bonding states (blue box in Fig. 2, which are primarily the

p_z orbitals of HITP) and higher-lying antibonding states (red box in Fig. 2, which are mainly composed of the $d_{xz}^{A,B,C}$ and $d_{yz}^{A,B,C}$ orbitals). Next considered are the SOC of the X atoms at the A, B, and C sites, which coupled to the π -bonding network, splitting the degenerate antibonding orbitals $d_{xz}^{A,B,C}$ and $d_{yz}^{A,B,C}$ into discrete energy bands marked as $d_{xz}^{1,2,3}$ and $d_{yz}^{1,2,3}$ in Fig. 2, respectively. The highest occupied electronic bands and thus the position of E_f in Fig. 2 are determined by n_X . If n_X is even, the exchange-split occupied bands are filled equally with electrons of both spins, and therefore $\mu=0 \mu_B$ in this material. On the contrary, if n_X is odd, in $\text{Ta}_3(\text{HITP})_2$ for instance, the $d_{z^2}^{A,B,C}$ bands of the three Ta atoms are each half filled, allowing for the FM spin alignment as the ground state of the system with $\mu=1 \mu_B$ per Ta atom. Similar phenomena occur in $\text{Re}_3(\text{HITP})_2$ ($d_{x^2-y^2}^{A,B,C}$ half-filled), $\text{Ir}_3(\text{HITP})_2$ ($d_{xz}^{1,2,3}$ half-filled) and $\text{Au}_3(\text{HITP})_2$ ($d_{yz}^{1,2,3}$ half-filled) as well. Such an effective magnetic exchange field (Δ) leads to an energy splitting between the majority (up, \uparrow) and minority (down, \downarrow) spin states. The strength of Δ , defined as half the energy splitting between the up- and down-spin states of the highest occupied band, decreases as n_X increases: it is 877 meV, 752 meV, 216 meV, and 0 meV for $X=\text{Ta}$, Re , Ir , and Au , respectively. The FM $\text{Ta}_3(\text{HITP})_2$, $\text{Re}_3(\text{HITP})_2$, and $\text{Ir}_3(\text{HITP})_2$ are candidate systems that can host QAH effect.

Having described the magnetic ground states of $X_3(\text{HITP})_2$ monolayers, we turn to their electronic properties. To realize the QAH phase in these materials, it is desirable to have their E_f within or close to the SOC-induced band gaps, which occur among the antibonding $d_{xz}^{1,2,3}$ (\uparrow or \downarrow) and $d_{yz}^{1,2,3}$ (\uparrow or \downarrow) bands. The Fermi levels of $\text{Ta}_3(\text{HITP})_2$, $\text{Re}_3(\text{HITP})_2$, and $\text{Ir}_3(\text{HITP})_2$ monolayers are relatively far below such band gap openings (see Supplemental Material [29]), so

it is imperative to elevate their E_f . Fortunately, the organic nature of these COFs offers the flexibility to engineer their electronic properties through chemical/structural manipulations. In this study, we use O atoms to fully or partially replace N atoms in the COF structure (Fig. 3) to introduce more electrons and consequently to raise E_f to the desired energy.

We demonstrate the successful realization of the QAH effect by such a modification in two COF structures, namely, $\text{Ta}_3(\text{HITP})_2$ and $\text{Ir}_3(\text{HITP})_2$. In $\text{Ta}_3(\text{HITP})_2$, all N atoms are substituted by O atoms [Fig. 3(a)]. This new COF-- $\text{Ta}_3(\text{C}_{18}\text{H}_{12}\text{O}_6)_2$ --is thermodynamically stable (see Supplemental Material [29]) and has a slightly larger lattice parameter than the original chemical formula- $\text{Ta}_3(\text{C}_{18}\text{H}_{12}\text{N}_6)_2$. It is FM as well because the total number of valence electrons in the new system is still odd. Its spontaneous magnetic moment, however, is greatly enhanced (3 μ_B per X atom) as compared to that of $\text{Ta}_3(\text{C}_{18}\text{H}_{12}\text{N}_6)_2$ (1 μ_B per X atom). The increase in μ can be understood from Fig. 3(a). Before the substitution, only the d_{z^2} orbital is half-filled in $\text{Ta}_3(\text{C}_{18}\text{H}_{12}\text{N}_6)_2$. After the substitution, four more electrons are introduced to the vicinity of each Ta atom as it has four nearest-neighbor O (or N) atoms. The added electrons in $\text{Ta}_3(\text{C}_{18}\text{H}_{12}\text{O}_6)_2$ first occupy the d_{z^2} orbital to make it fully filled and then half-fill the $d_{x^2-y^2}$, d_{xz} , and d_{yz} orbitals [Fig. 3(a)], leaving $\mu = 3 \mu_B$ per Ta atom. From Fig. 4(a), the strong magnetic exchange field in $\text{Ta}_3(\text{C}_{18}\text{H}_{12}\text{O}_6)_2$ results in a large separation between the up-spin (purple solid curves) and down-spin (green dashed curves) states of a given electronic band, pushing the down-spin electronic bands far away from E_f . Without considering SOC, the $|d_{yz}^{1,2}, \uparrow\rangle$ bands are degenerate at the Γ point, and the $|d_{yz}^{2,3}, \uparrow\rangle$ bands are degenerate at the K point, leaving a Dirac-cone. When SOC is turned on, such band degeneracies at the Γ and K points are broken, with two small band gap openings between $|d_{yz}^{1,2}, \uparrow\rangle$ (24 meV) and between $|d_{yz}^{2,3}, \uparrow\rangle$ (23 meV), respectively. Similar

phenomena occur in the $|d_{xz}^{1,2,3}, \uparrow\rangle$ bands, with band gap openings between $|d_{xz}^{1,2}, \uparrow\rangle$ and between $|d_{xz}^{2,3}, \uparrow\rangle$ (14 meV and 21 meV, respectively).

To further verify the capability of monolayer $\text{Ta}_3(\text{C}_{18}\text{H}_{12}\text{O}_6)_2$ for hosting a QAH phase, we look into its QAH conductivity σ_{xy} , expressed as $\sigma_{xy} = C \cdot e^2 / h$ where C is the Chern number, e is the elementary charge, and h is the Planck constant. C is the summation of the Chern numbers of electronic bands (C_n) that are occupied. (See Supplemental Material for the calculation of C_n [29].) The calculated C_n values for $|d_{yz}^1, \uparrow\rangle$, $|d_{yz}^2, \uparrow\rangle$, and $|d_{yz}^3, \uparrow\rangle$ in $\text{Ta}_3(\text{C}_{18}\text{H}_{12}\text{O}_6)_2$ are -1, 0, and 1, respectively; and those for $|d_{xz}^1, \uparrow\rangle$, $|d_{xz}^2, \uparrow\rangle$, and $|d_{xz}^3, \uparrow\rangle$ are 1, 0, and -1, respectively (Fig. 4). Since E_f in $\text{Ta}_3(\text{C}_{18}\text{H}_{12}\text{O}_6)_2$ falls between the $|d_{yz}^{1,2}, \uparrow\rangle$ bands, the sum of C_n for all occupied bands is -1, the same as C_n for $|d_{yz}^1, \uparrow\rangle$, leading to a finite σ_{xy} in the system [Fig. 4(c)], implying the capability of hosting the QAH phase.

Chemical modification is also applied to $\text{Ir}_3(\text{HITP})_2$, but with half of the N atoms replaced by O atoms while preserving the inversion symmetry around the central Ir atom [Fig. 3(b)]. The new COF structure-- $\text{Ir}_3(\text{C}_{18}\text{H}_{12}\text{N}_3\text{O}_3)_2$ --has two more electrons in the vicinity of each Ir atom than the original structure. The added electrons change the highest half-filled bands from the $d_{xz}^{1,2,3}$ orbitals to the $d_{yz}^{1,2,3}$ orbitals, but do not alter μ of the system (1 μ_B per Ir atom). At equilibrium, the $\text{Ir}_3(\text{C}_{18}\text{H}_{12}\text{N}_3\text{O}_3)_2$ monolayer is a semiconductor with a band gap around 0.53 eV without considering SOC, which results from the energy splitting between the $|d_{yz}^{1,2,3}, \uparrow\rangle$ and $|d_{yz}^{1,2,3}, \downarrow\rangle$ states [Fig. 5(a)]. Among the valence bands, the $|d_{yz}^{1,2}, \uparrow\rangle$ bands are degenerate at the K point and the $|d_{yz}^{2,3}, \uparrow\rangle$ bands are degenerate at the Γ point; while at the conduction band edge, the

$|d_{yz}^{1,2}, \downarrow\rangle$ bands are degenerate at the Γ point and the $|d_{yz}^{2,3}, \downarrow\rangle$ bands are degenerate at the K point. These degeneracies are broken by SOC [Fig. 5(b)]. The SOC-induced band gaps between $|d_{yz}^{2,3}, \uparrow\rangle$ and between $|d_{yz}^{1,2}, \downarrow\rangle$ are each $\approx 8-9$ meV; however, those between $|d_{yz}^{1,2}, \uparrow\rangle$ and between $|d_{yz}^{2,3}, \downarrow\rangle$ are 0 meV or even negative. The Chern numbers of $|d_{yz}^{1,2,3}, \uparrow\rangle$ are 0, 1, and -1, respectively; and those of $|d_{yz}^{1,2,3}, \downarrow\rangle$ are 1, 0, and -1, respectively. From Fig. 5(b), the sum of C_n for all occupied bands and thus the Hall conductivity in the system is 0, since E_f is between the $|d_{yz}^3, \uparrow\rangle$ and $|d_{yz}^1, \downarrow\rangle$ bands, meaning a topologically trivial state. However, if E_f of the $\text{Ir}_3(\text{C}_{18}\text{H}_{12}\text{N}_3\text{O}_3)_2$ monolayer is lowered to between the $|d_{yz}^{2,3}, \uparrow\rangle$ bands or raised to between the $|d_{yz}^{1,2}, \downarrow\rangle$ bands [yellow areas in Figs. 5(b) and (c)], C of the system will become 1, indicating a finite σ_{xy} [Figs. 5(d) and (e)]. Such Fermi-level tuning could be achieved by a gating voltage that injects electrons or holes into the system. The requisite injected charge carrier density in $\text{Ir}_3(\text{C}_{18}\text{H}_{12}\text{N}_3\text{O}_3)_2$ is estimated to be $2.3 \times 10^{13} \text{ cm}^{-2}$. This should be viable, since higher carrier densities ($> 10^{14} \text{ cm}^{-2}$) have been experimentally demonstrated in monolayer graphene samples by electric gating technologies [40,41].

We also perform GGA+U calculations to verify that the QAH phases in $\text{Ta}_3(\text{C}_{18}\text{H}_{12}\text{O}_6)_2$ and $\text{Ir}_3(\text{C}_{18}\text{H}_{12}\text{N}_3\text{O}_3)_2$ are preserved, and the on-site Coulomb interactions for the $5d$ elements only influence the SOC induced band gaps to some degrees. Detailed information is given in Supplemental Material [29]. The band gap is 8-23 meV in $\text{Ta}_3(\text{C}_{18}\text{H}_{12}\text{O}_6)_2$ monolayer and 8-18 meV in $\text{Ir}_3(\text{C}_{18}\text{H}_{12}\text{N}_3\text{O}_3)_2$ monolayer, depending on the choice of the Coulomb term. Using 26 meV equivalent to 300 K as a rough estimate, the QAH phase in $\text{Ta}_3(\text{C}_{18}\text{H}_{12}\text{O}_6)_2$ is expected to be robust at temperatures between 81K and 277 K, and that in $\text{Ir}_3(\text{C}_{18}\text{H}_{12}\text{N}_3\text{O}_3)_2$ is expected to be

robust at temperatures between 104 K and 208 K. This is much higher than the temperature (<100 mK) at which current QAH experiments are conducted [8-10]. Furthermore, the FM ordering temperature in $\text{Ta}_3(\text{C}_{18}\text{H}_{12}\text{O}_6)_2$ and $\text{Ir}_3(\text{C}_{18}\text{H}_{12}\text{N}_3\text{O}_3)_2$ is large enough to retain the QAH phases in the above-mentioned temperature ranges (see Supplemental Material [29]). Finally, the viability of synthesizing similar COF structures $[\text{Ni}_3(\text{HITP})_2]$ and $[\text{Cu}_3(\text{HITP})_2]$ has been experimentally demonstrated [24,25]. Taken together, these three points make $\text{Ta}_3(\text{C}_{18}\text{H}_{12}\text{O}_6)_2$ and $\text{Ir}_3(\text{C}_{18}\text{H}_{12}\text{N}_3\text{O}_3)_2$ monolayers very promising in practical QAH applications.

Acknowledgements:

This work is supported by the grants EFMA-542879, CMMI-1363203 and CBET-1235870 from the US National Science Foundation. YK acknowledges support from NSF grant DMR-1120901 and computational support from the HPCMO of the U.S. DOD and the NERSC of the U.S. DOE. AMR acknowledges support from the U.S. Office of Naval Research, under grant N00014-14-1-0761. The authors acknowledge useful discussions with Prof. Charles Kane.

References:

- [1] C. L. Kane and E. J. Mele, Phys. Rev. Lett. **95**, 226801 (2005).
- [2] B. A. Bernevig, T. L. Hughes, and S.-C. Zhang, Science **314**, 1757 (2006).
- [3] M. Z. Hasan and C. L. Kane, Rev. Mod. Phys. **82**, 3045 (2010).
- [4] B. Yan and S.-C. Zhang, Rep. Prog. Phys. **75**, 096501 (2012).
- [5] Y. Ando, J. Phys. Soc. Jpn **82**, 102001 (2013).
- [6] S. Oh, Science **340**, 153 (2013).
- [7] Z. F. Wang, N. Su, and F. Liu, Nano Lett. **13**, 2842 (2013).
- [8] C.-Z. Chang *et al.*, Science **340**, 167 (2013).
- [9] J. G. Checkelsky, R. Yoshimi, A. Tsukazaki, K. S. Takahashi, Y. Kozuka, J. Falson, M. Kawasaki, and Y. Tokura, Nature Phys. **10**, 731 (2014).
- [10] X. Kou *et al.*, Phys. Rev. Lett. **113**, 137201 (2014).
- [11] C.-Z. Chang *et al.*, Nature Mater **14**, 473 (2015).
- [12] C.-X. Liu, X.-L. Qi, X. Dai, Z. Fang, and S.-C. Zhang, Phys. Rev. Lett. **101**, 146802 (2008).
- [13] Z. Qiao, S. A. Yang, W. Feng, W.-K. Tse, J. Ding, Y. Yao, J. Wang, and Q. Niu, Phys. Rev. B **82**, 161414 (2010).
- [14] H. Zhang, C. Lazo, S. Blügel, S. Heinze, and Y. Mokrousov, Phys. Rev. Lett. **108**, 056802 (2012).
- [15] M. Ezawa, Phys. Rev. Lett. **109**, 055502 (2012).
- [16] X.-L. Zhang, L.-F. Liu, and W.-M. Liu, Sci. Rep. **3**, 2908 (2013).
- [17] K. F. Garrity and D. Vanderbilt, Phys. Rev. Lett. **110**, 116802 (2013).

- [18] Z. Qiao, W. Ren, H. Chen, L. Bellaiche, Z. Zhang, A. H. MacDonald, and Q. Niu, Phys. Rev. Lett. **112**, 116404 (2014).
- [19] G. Xu, J. Wang, C. Felser, X.-L. Qi, and S.-C. Zhang, Nano Lett. **15**, 2019 (2015).
- [20] Z. F. Wang, Z. Liu, and F. Liu, Phys. Rev. Lett. **110**, 196801 (2013).
- [21] M. Yankowitz, J. Xue, D. Cormode, J. D. Sanchez-Yamagishi, K. Watanabe, T. Taniguchi, P. Jarillo-Herrero, P. Jacquod, and B. J. LeRoy, Nature Phys. **8**, 382 (2012).
- [22] C. R. Woods *et al.*, Nature Phys. **10**, 451 (2014).
- [23] J. W. Colson and W. R. Dichtel, Nature Chem. **5**, 453 (2013).
- [24] D. Sheberla, L. Sun, M. a. Blood-Forsythe, S. Er, C. R. Wade, C. K. Brozek, A. Aspuru-Guzik, and M. Dincă, J. Am. Chem. Soc. **136**, 8859 (2014).
- [25] M. G. Campbell, D. Sheberla, S. F. Liu, T. M. Swager, and M. Dincă, Angew. Chem. Int. Ed. **54**, 4349 (2015).
- [26] G. Kresse and J. Furthmüller, Phys. Rev. B **54**, 11169 (1996).
- [27] P. E. Blochl, Phys. Rev. B **50**, 17953 (1994).
- [28] J. P. Perdew, K. Burke, and M. Ernzerhof, Phys. Rev. Lett. **77**, 3865 (1996).
- [29] See Supplemental Material at [URL will be inserted by publisher], which includes Refs. [30-37].
- [30] S. L. Dudarev, G. A. Botton, S. Y. Savrasov, C. J. Humphreys, and A. P. Sutton, Phys. Rev. B **57**, 1505 (1998).
- [31] S. J. Moon, H. Jin, K. W. Kim, W. S. Choi, Y. S. Lee, J. Yu, G. Cao, A. Sumi, H. Funakubo, C. Bernhard, and T. W. Noh, Phys. Rev. Lett. **101**, 226402 (2008).
- [32] I. I. Mazin, S. Manni, K. Foyevtsova, H. O. Jeschke, P. Gegenwart, and R. Valentí, Phys. Rev. B **88**, 035115 (2013).

- [33] B. J. Kim, H. Jin, S. J. Moon, J.-Y. Kim, B.-G. Park, C. S. Leem, J. Yu, T. W. Noh, C. Kim, S.-J. Oh, J.-H. Park, V. Durairaj, G. Cao, and E. Rotenberg, *Phys. Rev. Lett.* **101**, 076402 (2008).
- [34] X. Wan, A. M. Turner, A. Vishwanath, and S. Y. Savrasov, *Phys. Rev. B* **83**, 205101 (2011).
- [35] E. Şaşıoğlu, C. Friedrich, and S. Blügel, *Phys. Rev. B* **83**, 121101(R) (2011).
- [36] W. Sun, W. Luo, and R. Ahuja, *J. Mater. Sci.* **47**, 7615 (2012).
- [37] N. J. Lane, M. W. Barsoum, and J. M. Rondinelli, *EPL* **101**, 57004 (2013).
- [38] B. Zhao, J. Zhang, W. Feng, Y. Yao, and Z. Yang, *Phys. Rev. B* **90**, 201403(R) (2014).
- [39] S. Chen, J. Dai, and X. C. Zeng, *Phys. Chem. Chem. Phys.* **17**, 5954 (2015).
- [40] D. K. Efetov and P. Kim, *Phys. Rev. Lett.* **105**, 256805 (2010).
- [41] J. Ye, M. F. Craciun, M. Koshino, S. Russo, S. Inoue, H. Yuan, H. Shimotani, A. F. Morpurgo, and Y. Iwasa, *Proc. Natl. Acad. Sci. U.S.A.* **108**, 13002 (2011).

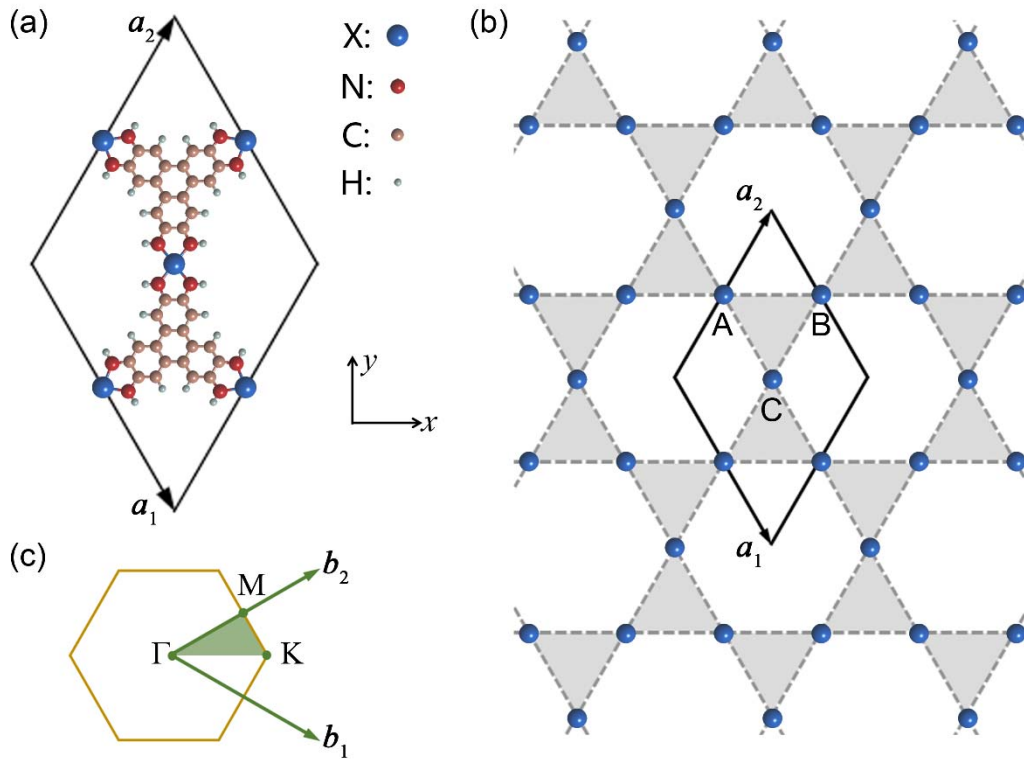


Figure 1 (a) Top view of a unit cell of $X_3(\text{HITP})_2$ monolayer with lattice vectors a_1 and a_2 in the xy -plane; (b) a schematic showing that X atoms form a kagome lattice with three atomic sites A, B, and C in a unit cell; and (c) the first Brillouin zone of the structure, with reciprocal lattice vectors b_1 and b_2 and high-symmetry points Γ , M, and K.

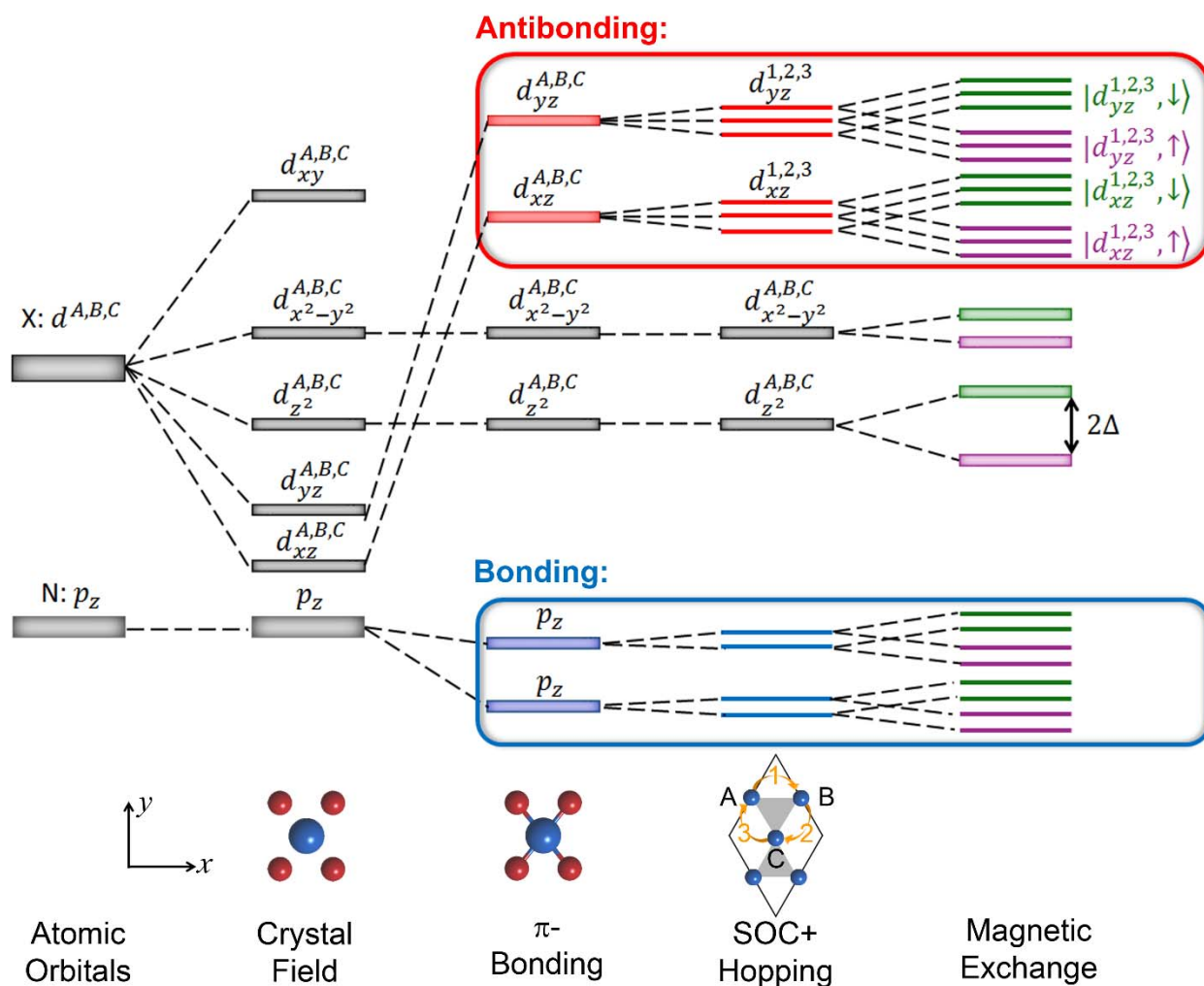


Figure 2 A schematic of the electronic band structure around the E_F that explains the origin of ferromagnetism in certain $X_3(HITP)_2$ monolayers with magnetic exchange field Δ .

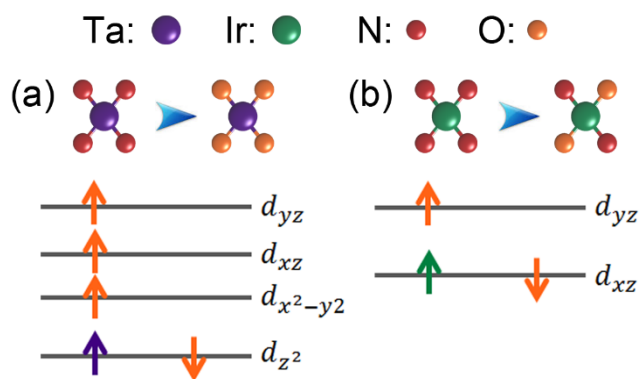


Figure 3 Schematic of the changes in crystal structure and electron filling configuration of $X_3(\text{HITP})_2$ when (a) all N in $\text{Ta}_3(\text{C}_{18}\text{H}_{12}\text{N}_6)_2$ are replaced by O, resulting in the $\text{Ta}_3(\text{C}_{18}\text{H}_{12}\text{O}_6)_2$ structure, and (b) half of N atoms in $\text{Ir}_3(\text{C}_{18}\text{H}_{12}\text{N}_6)_2$ are replaced by O, resulting in the $\text{Ir}_3(\text{C}_{18}\text{H}_{12}\text{N}_3\text{O}_3)_2$ structure.

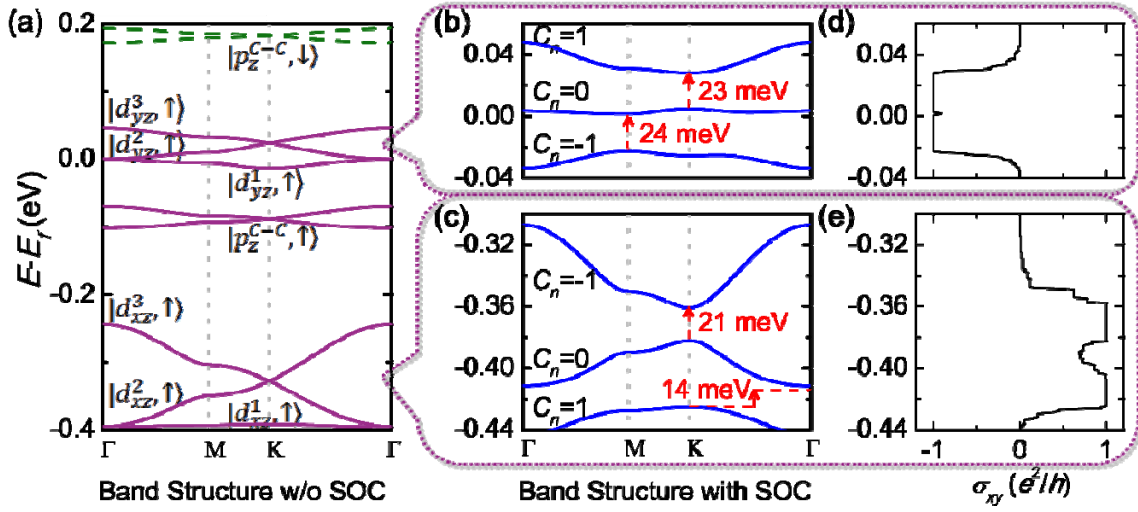


Figure 4 Band structure and σ_{xy} of Ta₃(C₁₈H₁₂O₆)₂: (a) the band structure without considering SOC; (b) and (c) the band structure after turning on SOC for the $|d_{yz}^{1,2,3}, \uparrow\rangle$ and the $|d_{xz}^{1,2,3}, \uparrow\rangle$ bands, respectively; and (d) and (e) σ_{xy} of Ta₃(C₁₈H₁₂O₆)₂ as a function of the Fermi energy tuning corresponding to (b) and (c), respectively.

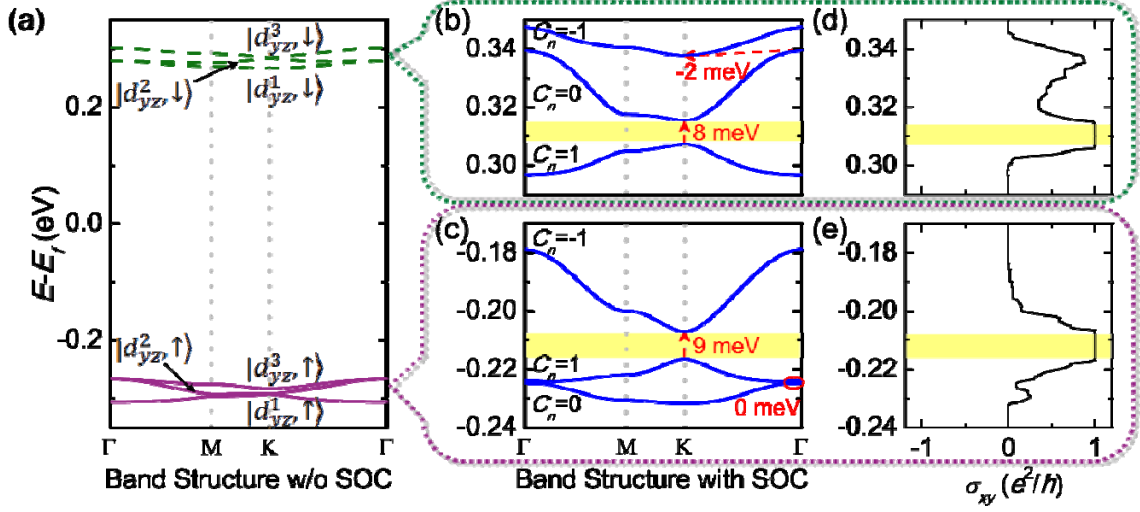


Figure 5 Band structure and σ_{xy} of $\text{Ir}_3(\text{C}_{18}\text{H}_{12}\text{N}_3\text{O}_6)_2$: (a) the band structure without considering SOC; (b) and (c) the band structure after turning on SOC for the $|d_{yz}^{1,2,3}, \downarrow\rangle$ and the $|d_{yz}^{1,2,3}, \uparrow\rangle$ bands, respectively; and (d) and (e) σ_{xy} of $\text{Ir}_3(\text{C}_{18}\text{H}_{12}\text{N}_3\text{O}_6)_2$ as a function of the Fermi energy tuning corresponding to (b) and (c), respectively.